NANO LETTERS

pubs.acs.org/NanoLett Letter

Emergent Ferromagnetism in $CaRuO_3/CaMnO_3$ (111)-Oriented Superlattices

Margaret Kane,* Churna Bhandari,* Megan E. Holtz, Purnima P. Balakrishnan, Alexander J. Grutter, Michael Fitzsimmons, Chao-Yao Yang, Sashi Satpathy, Durga Paudyal, and Yuri Suzuki*

Cite This: *Nano Lett.* 2024, 24, 2567−2573 Read Online

ACCESS | Metrics & More | Article Recommendations | Supporting Information

ABSTRACT: The boundary between $CaRuO_3$ and $CaMnO_3$ is an ideal test bed for emergent magnetic ground states stabilized through interfacial electron interactions. In this system, nominally antiferromagnetic and paramagnetic materials combine to yield interfacial ferromagnetism in $CaMnO_3$ due to electron leakage across the interface. In this work, we show that the crystal symmetry at the surface is a critical factor determining the nature of the interfacial interactions. Specifically, by growing $CaRuO_3/CaMnO_3$ heterostructures along the (111) instead of the (001) crystallographic axis, we achieve a 3-fold enhancement of the magnetization and involve the $CaRuO_3$ layers in the ferromagnetism, which now spans both constituent materials. The stabilization of a net magnetic moment in $CaRuO_3$ through strain effects has been long-sought but never consistently achieved, and our observations demonstrate the importance of interface engineering in the development of new functional heterostructures.

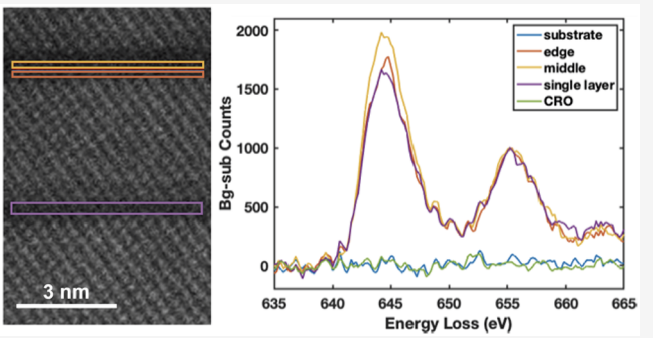

KEYWORDS: *emergent magnetism, complex oxides, superlattices, ruthenatess, manganites*

Low dimensional ferromagnetism is of fundamental and technological interest, as the isolation of a net moment to the interface of a nonmagnetic material presents opportunities for fundamental spin transport and novel spin-based device studies.[1−6] The emergent interfacial ferromagnetism in (001)-oriented $CaRuO_3/CaMnO_3$ (CRO/CMO) superlattices is attributed to the leakage of itinerant electrons from the metallic CRO into the insulating antiferromagnetic CMO layer, acting as a fractional charge transfer to Mn ions.[7−13] Theoretical studies[12] and electron energy loss spectroscopy (EELS)[9] indicate that these itinerant electrons stabilize a weak double exchange interaction among the interfacial Mn atoms of the CMO. The charge transfer magnitude decays rapidly away from the interface so that the ferromagnetic signal is isolated to the first unit cell of the CMO, where competition between superexchange and double exchange results in a canted moment of 0.85−1.0 μ_B/Mn.

This emergent magnetic ground state can be tuned by applying an electric field, modulating the double exchange to enable the suppression or full alignment of the surface Mn^{4+} ions for a maximum interfacial moment of 2.5−3.0 μ_B/Mn.[11] Alternatively, interfacial structural symmetry can modify the interfacial magnetic moments of (001) CRO/CMO and the closely related (001) LNO/CMO system.[10,14] Specifically, changes in the tilt and rotation pattern of the oxygen octahedra across the interface have yielded 2-fold variations in the interfacial magnetization.[9,10] These observations suggest that changing the crystallographic growth axis could yield dramatic changes in the magnetic ground state. In fact, it has been previously demonstrated in heterostructures such as $LaFeO_3/(La,Sr)MnO_3$ that (111)-oriented interfaces can enhance the interlayer coupling, yielding a larger emergent magnetization and modifying the antiferromagnetic spin textures.[15] These observations have been attributed to the change in symmetry and greater degree of octahedral connectivity across the interface.[16]

The realization of CRO/CMO superlattices in the (111) direction offers a unique opportunity to exploit the interplay between charge transfer and octahedral connectivity to stabilize novel emergent magnetic ground states at atomically precise interfaces. Specifically, we expect modified orbital hybridization and, consequently, modified exchange interactions at the interfaces. Further, the G-type antiferromagnetic order of CMO manifests ferromagnetically aligned Mn moments along the (111) planes,[17] which is likely to enhance

Received: November 28, 2023
Revised: February 6, 2024
Accepted: February 9, 2024
Published: February 17, 2024

https://doi.org/10.1021/acs.nanolett.3c04623
Nano Lett. 2024, 24, 2567−2573

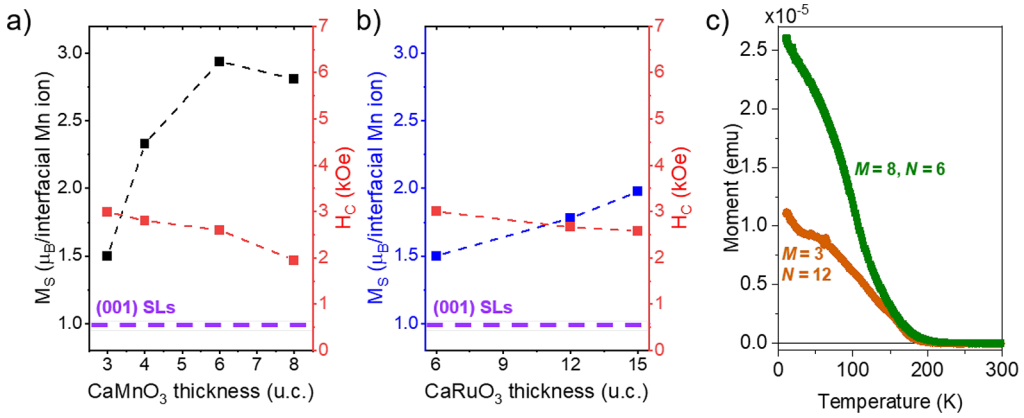

Figure 1. SQUID magnetometry measurements of CMO/CRO(111) superlattices (SLs), saturated moment of SLs with (a) varying CMO thickness (3−8 u.c.) and constant CRO thickness of 6 u.c. and (b) varying CRO thickness (6−15 u.c.) and constant CMO thickness of 3 u.c.. (c) Magnetization with temperature for $[CMO_M/CRO_N$ superlattices, field cooled at H = 5 T, measurement taken at H = 5 mT. 1 emu = 1 mA m^2.

the magnitude of the emergent magnetism. Lastly, the (111) interfaces drive unique strain symmetries that could stabilize the altered magnetism and unique spin textures. Therefore, the (111) orientation may give rise to even more exotic emergent long-range magnetic order.

In this Letter, we examine a series of $[(CaRuO_3)_N/(CaMnO_3)_M]_5$ superlattices (SLs) grown on (111) $LaAlO_3$ substrates by pulsed laser deposition (see Methods in the Supporting Information). Thicknesses were varied for both CRO (N = 6−15 u.c.) and CMO (M = 3−8 u.c.), where we define 1 u.c. (unit cell) as the distance between adjacent (111) planes; d_{111} = 0.223 nm. We demonstrate a novel emergent ferromagnetic ground state arising from the interplay of interfacial charge transfer and interfacial strain symmetry driven distortions. Surprisingly, the large resultant ferromagnetic moment appears to originate from both Mn and Ru ions, and the net magnetization is not exclusively confined to the first unit cell, as in the (001) orientation. This picture of the magnetism is supported by *ab initio* calculations and structural and magnetic depth profiles extracted using polarized neutron reflectometry. The enhanced Curie temperature of 175 K, compared to 100 K observed in the (001)-oriented system points to stronger exchange interactions in the (111) system. Scanning transmission electron microscopy (STEM) measurements and X-ray reflectivity (XRR) spectra reveal sharp interfaces. Together the magnetic and structural evidence points to a new material phase space for low-dimensional ferromagnetism driven by charge transfer and strain symmetry.

All SLs exhibited smooth surface morphology, and XRR measurements (Supporting Information Figure S1) confirmed the low roughness and intended layer structure of the CRO/CMO superlattices. Specifically, the interfacial and surface roughnesses were found to be below 0.7 nm for all samples, independent of the measured net magnetism. We note that XRR measurements include contributions from long-range thickness variations, conformal roughness, and intermixing across tens of micrometers, so that roughnesses extracted by fitting XRR data represent an upper bound. Correspondingly, RMS roughnesses measured by 1 μm × 1 μm AFM scans were lower and ranged from 0.24 to 0.66 nm. Both AFM and XRR measurements are comparable to those measured from (001)-oriented SLs previously, and the sub-nanometer roughnesses observed demonstrate high-quality interfaces in our (111)-oriented SLs. Critically, the roughness remained fairly constant with increasing film thickness, indicating that an increase in intermixing as the layer thickness increased was unlikely.

For a more local examination of the interface quality, we performed scanning transmission electron microscopy (STEM). STEM scans of a $[(CMO)_3/(CRO)_{15}]_5$ superlattice confirm high-quality interfaces and distinct layers in our superlattices. As seen in Figure S2, the CMO layer thickness shows some variation from 2 to 4 u.c., possibly due to the roughness of the $LaAlO_3$ substrate or deposition of incomplete layers. This measurement supports the XRR data that indicate high-quality (111) superlattices.

SQUID magnetometry from (111) CRO/CMO SLs with varying CRO and CMO thicknesses revealed ferromagnetism in all samples but with moments larger than those of the (001)-oriented system. Further, we observed an unexpected thickness dependence of the saturation magnetization M_S. Specifically, M_S increased with both CRO and CMO thicknesses, as shown in Figure 1a,b. At a constant CRO thickness of N = 6 u.c., increasing CMO thickness from M = 3−8 u.c. increases M_S from 1.5 μ_B/interfacial Mn for M = 3 to 2.8−2.9 μ_B/interfacial Mn for M = 6, 8 (Figure 1a), where the reported moment was normalized by the number of interfacial Mn atoms at CRO/CMO interfaces. This evolution of the Mn moment/interface contrasts starkly with the (001) SL value shown in Figure 1 as a dashed line. The large magnetization enhancement suggests that the emergent magnetization may not be confined to the interfacial Mn. Because the moment/interfacial Mn saturates at M = 6, we postulate that three layers of the CMO at the interface contribute to the magnetization. This is supported by the lack of exchange bias in all samples, suggesting that an insufficient quantity of antiferromagnetically aligned CMO to enable pinning of the ferromagnetic moment. Similar to the case for (001)-oriented samples, the coercive field (H_c) slowly decreases with increasing CMO thickness. Unlike (001)-oriented samples, we did not observe any even/odd dependence on the magnetic moment nor any exchange bias of the magnetization loops.[9]

In a second series of SLs, CMO thickness was held constant at M = 3 u.c. while CRO thickness was varied from N = 3 to 15 u.c. The moment increased from 1.5 μ_B/interfacial Mn ion for N = 3 to 2.0 μ_B/interfacial Mn for N = 15. While the total moment increase per CRO unit cell was much smaller than that for increasing CMO layer thickness, the net moment continued to increase up to N = 15. A linear fit of these data

https://doi.org/10.1021/acs.nanolett.3c04623
Nano Lett. 2024, 24, 2567−2573

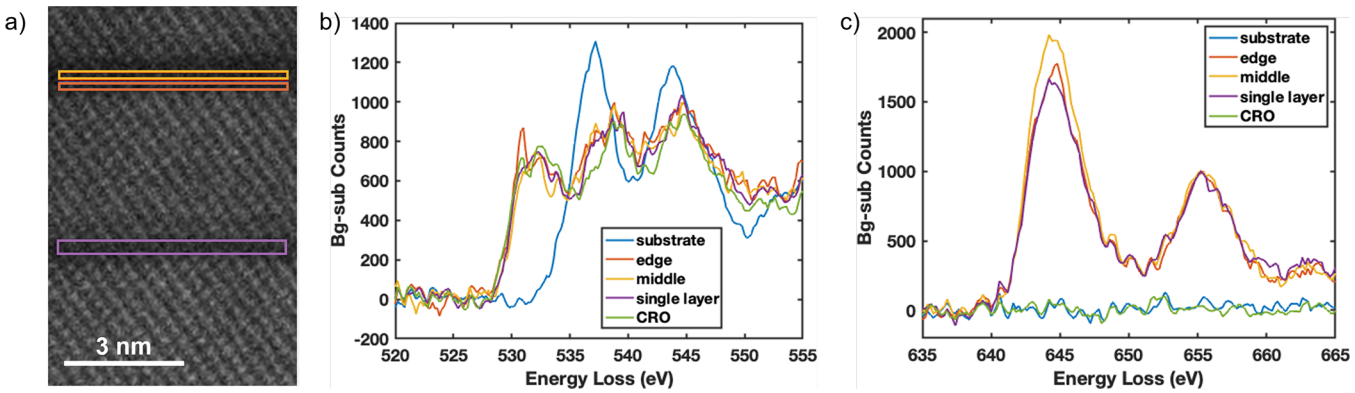

Figure 2. STEM-EELS measurements of a $[(CMO)_3/(CRO)_{15}]_5$ superlattice. (a) STEM scan with colored boxes to indicate scan location, (b) O K-edge measurements for various scans, and (c) Mn L-edge measurements for various scans.

points suggests that each additional layer adds 0.05 μ_B/Ru. This trend may indicate a small ferromagnetic contribution from the CRO layers, which was not observed in (001)-oriented SLs.[7]

Temperature-dependent magnetization measurements (Figure 1c) revealed an approximately 175 K Curie temperature (T_C) for all samples, consistent with the onset of hysteretic magnetoresistance and an anomalous Hall effect in electrical transport measurements (see Supporting Information). This T_C is higher than the Néel temperature of bulk CMO (T_N = 123 K)[18] but within the 150−210 K range observed for $CaRu_xMn_{1-x}O_3$.[19−22] However, if the increase in the measured moment was due to changes in the degree of intermixing, we would expect changes in T_C corresponding to trends in the measured moment. Instead, T_C is independent of both the CMO and CRO thickness, favoring a uniform interfacial origin. A similar T_C enhancement observed in CMO/$LaNiO_3$ SLs from T = 125 K in (001)-oriented SLs to T = 200 K in (111)-oriented SLs suggests that the Néel temperature of CMO depends on growth direction.[23] In fact, past work on (Sr,Ca)MnO_3 and (Sr,Ba)MnO_3 shows that the Néel temperature is enhanced by structural distortions which increase the Mn−O−Mn bond angle and orbital overlap, with maximal values exceeding 230 K.[24] We speculate that (111)-oriented strain and interface interactions play a similar role here so that growth in the [111] direction could serve as a powerful tool to enhance T_C of G-type antiferromagnets.

To understand the origins of the enhanced magnetization in CRO/CMO(111), we studied the evolution of the charge transfer from the CRO to CMO as a function of layer thickness. Specifically, we probed the chemical valence using electron energy loss spectroscopy (EELS) and X-ray absorption spectroscopy (XAS). The EELS measurements were taken both at the interface and the middle of the CMO layers (see Figure 2a) within a $[(CMO)_3/(CRO)_{15}]_5$ sample, at energies corresponding to the O K-edge and the Mn L-edge, shown in Figure 2b,c, respectively. Surprisingly, the Mn L_3 appears more intense relative to the L_2 near the middle of the CMO layer, indicating a lower Mn valence and consequently higher charge transfer near the CMO center. Such a finding is counterintuitive, and we propose that transferred electrons from both top and bottom interfaces may contribute to the signal near the CMO center. Examining the L_3/L_2 separation and intensity ratio of the EELS measurements yields valences of Mn^{3+} and ($Mn^{3.5+}$) at the center and interface, respectively. Recalling that previously reported EELS measurements on (001)-oriented systems were consistent with a valence shift of 0.1 (i.e., from Mn^{4+} to $Mn^{3.9+}$ at the interface,[9] the enhancement of emergent magnetism in (111)-oriented SLs is attributed to increased charge transfer relative to the (001) orientation.

We confirmed these results with XAS and X-ray magnetic circular dichroism (XMCD) on a $[(CMO)_8/(CRO)_6]_5$ SL (Figure 3), explicitly resolving the spectroscopic signatures of

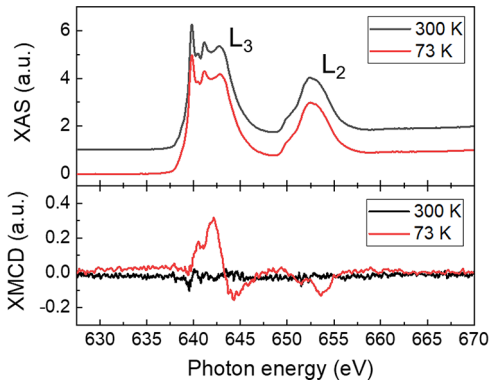

Figure 3. (Top) Mn L-edge X-ray absorption and (bottom) X-ray magnetic circular dichroism measurements of $[(CMO)_8/(CRO)_6]_5$ taken at 73 and 300 K with H = 0.7 T.

Mn^{2+}, Mn^{3+}, and Mn^{4+}. Based on the integrated L_3/L_2 intensity ratio, we estimated an average valence of approximately $Mn^{3.2+}$, in excellent agreement with EELS. The Mn XMCD spectra at T = 73 K (Figure 3) explicitly identify ferromagnetism on the Mn ions in these (111) SLs, whereas no XMCD signal was observed at 300 K. Unfortunately, XMCD measurements at the Ru edge were not possible due to the low X-ray interaction cross-section of the Ru M-edge. We must therefore use alternative methods, such as polarized neutron reflectometry (PNR), to understand the contribution of Ru to the observed emergent magnetization.

PNR measurements were performed on a pair of $[(CMO)_3/(CRO)_N]_5$ SLs, where N = 12, 15, in order to separate the contributions of the CMO and CRO layers to the overall magnetization of the samples. Both samples were fit simultaneously to a model with linked parameters. For example, the nuclear (but not magnetic) scattering length density (SLD) of the CRO layers were presumed to be uniform within each layer, between layers, and across both samples. Any net CRO magnetization was confined to the 3

https://doi.org/10.1021/acs.nanolett.3c04623
Nano Lett. 2024, 24, 2567−2573

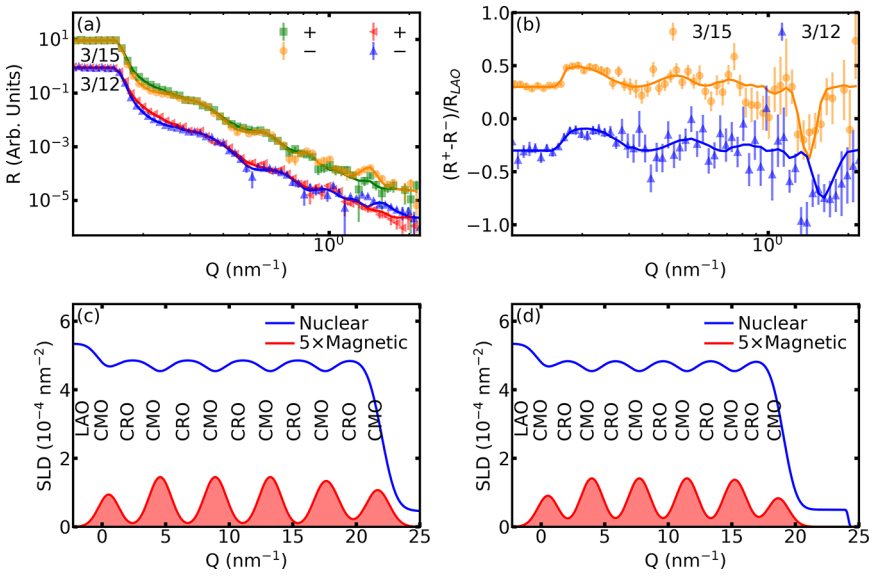

Figure 4. (a) Polarized neutron reflectometry measurements performed on (111)-oriented $[(CMO)_3/(CRO)_{15}]_5$ and $(CMO)_3/(CRO)_{12}]_5$ samples alongside theoretical fits. (b) Fresnel-normalized spin differences associated with the same samples, alongside the same theoretical curves. (c) Best-fit nuclear and magnetic SLD profiles for the 3/15 SL. (d) Best-fit nuclear and magnetic SLD profiles for the 3/12 SL. Error bars represent ±1 standard deviation.

u.c. layer at the interface. The CMO magnetic SLD was allowed to vary between samples but was uniform and constant within each CMO sublayer (see the Supporting Information for modeling details). Model optimization under these constraints yields an excellent fit to the data with reduced χ^2 = 1.35. Interfacial roughness parameters, which probe the combined effects of conformal roughness, intermixing, and thickness variations, were approximately 0.8 nm, in excellent agreement with the XRR analysis. The fitted spin-dependent reflectivities support the presence of a modulated ferromagnetic moment concentrated in the CMO layers, as shown in Figure 4. For the N = 12 sample, the integrated magnetic SLD over all layers fit to the PNR data corresponded to 1.66 ± 0.1 μ_B normalized per interfacial Mn ion (unless otherwise noted, uncertainties correspond to ±1 standard deviation). Similarly, fitting the N = 15 sample data yields a moment of 1.72 ± 0.1 μ_B per interfacial Mn ion. Both the extracted values and the thickness trend are in good agreement with the values and trends shown in Figure 1. The increase in the total moment between the two samples with identical CMO layer thickness further supports the emergence of ferromagnetism polarization in the CRO layers.

The PNR results support the stabilization of magnetic polarization in the CRO layers. The fitted CRO magnetization within 3 u.c. of the interface was 220(60) kA/m (1.3(0.2) μ_B/Ru). Fitting the data with counterfactual models in which the CRO magnetization is either constrained to be zero or uniformly distributed through the layer reduces the fit quality to approximately 1.42. We therefore conclude that PNR favors net magnetization originating in the CRO layers and localized near the interface. However, PNR cannot precisely determine the thickness of the magnetized layer or the shape of the falloff away from the interface. Additional details on PNR fitting and alternative models can be found in the Supporting Information.

To place our experimental results into theoretical context, we performed density functional theory (DFT) calculations on three superlattice geometries: (1) three layers of CMO and six layers of CRO (3CMO/6CRO); (2) three layers of CMO and 12 layers of CRO (3CMO/12CRO); and (3) six layers of CMO and six layers of CRO (6CMO/6CRO) along the body diagonal [111] direction of the pseudoubic perovskite unit cell. We constrained the in-plane lattice constant to match the substrate $LaAlO_3$(111) and preserved the experimental volume of each unit cell and then optimized the atomic positions with force less than 10^{-3} eV/Å.

Two solutions with similar energies were obtained for odd layers of CMO and are shown schematically in Figure 5. Both

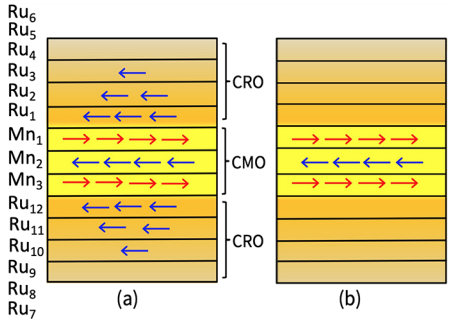

Figure 5. Schematic diagram showing spin polarized electron gas in MCMO/NCRO (M = 3 and N = 12) [111] superlattice in (a) type I and (b) type II solutions. As indicated from the panels, the spin polarization quickly becomes zero as one moves away from the interface.

solutions have robust, antiferromagnetically aligned MnO layers but differ in the magnetic moments of the Ru atoms in the CRO layers. The first solution (type I) includes a significant magnetic moment induced on Ru ions in proximity to the interface with CMO. The second solution (type II) exhibits no magnetic moment in the ruthenium. While the two solutions have similar net moment, the type I solution is lower energy (see Table 1), implying that ferromagnetism is likely to be induced in the CRO layers. In all superlattice models, the Ru moment decreases quickly away from the CMO/CRO interface. Values are presented in Table 1 and partial densities

https://doi.org/10.1021/acs.nanolett.3c04623
Nano Lett. 2024, 24, 2567−2573

Table 1. Magnetic Moments of Mn and Ru (Units of μ_B) in the *M*CMO/*N*CRO Superlattices, with (*M*, *N*) = (3, 6) or (3, 12)[a]

*M*CMO/*N*CRO	$Mn_{1,3}$, Mn_2	$Ru_{1,6}$, $Ru_{2,5}$, $Ru_{3,4}$	μ_{tot}	Energy
(3,6) Type I	−2.68, 2.33	1.22, 1.07, 0.05	3.81	−0.09
(3,6) Type II	−2.66, 2.43	−0.02, −0.10, 0.00	−3.58	0.00
*M*CMO/*N*CRO	$Mn_{1,3}$, Mn_2	$Ru_{1,12}$, $Ru_{2,11}$, $Ru_{3,10}$, $Ru_{4,9}$, $Ru_{5,8}$, $Ru_{6,7}$	μ_{tot}	Energy
(3,12) Type I	−2.68, 2.35	1.15, 1.09, 0.03, 0.00, −0.04, 0.08	3.84	−0.20
(3,12) Type II	−2.64, 2.34	−0.01, −0.14, 0.11, −0.05, 0.01, 0.03	−3.60	0.00

[a]The net magnetization of the entire superlattice is indicated by μ_{tot}, and the total energy (in eV) is with respect to the type II structure. The subscripts on the atoms, i = 1...*M* or *N*, denote the individual layers as indicated in Figure 5. The paired indices indicate symmetry-equivalent atoms.

of states for each atom are shown in Figure S4 in the Supporting Information.

For both geometries with three CMO layers, CMO maintains G-type antiferromagnetic ordering, but the moment on Mn sites in adjacent (111) layers are not equal. The middle layer Mn has a moment 0.34 μ_B smaller than the interfacial layers, yielding a net moment of about 1.9 μ_B per interface. In the 6CMO/6CRO case, the structure is not symmetric, and we consequently find a nonsymmetric solution in the magnetic moment. We find that the two Mn layers adjacent to one of the interfaces are ferromagnetically coupled, while the remaining layers are antialigned, with the total moment per interface increasing to 2.3 μ_B. Thus, predictions in all cases match the experimentally observed increase in interfacial moments relative to the (001) orientation. Note that this model does not include considerations for Mn-moment canting, as would be expected from itinerant electron exchange. For the (111) interface, the Mn 3d states are much more delocalized (see Figure S4 layer resolved partial density of states) in contrast to the CMO/CRO(001) interface.[25] We find that all three CMO layers acquire a similar number of itinerant electrons leaked from the CRO side, ≈0.09 and ≈0.06 electrons for 3CMO/6CRO and 3CMO/12CRO, respectively. In the 6CMO/6CRO SL, the average charge acquired by interfacial Mn is 0.093 electron, while the middle Mn layers acquire ≈0.06 electron per Mn. The charge transfer decreases away from the interface, but it is not obvious how far the itinerant electrons leak in the CMO layers.

We now combine all of our observations into a complete picture of the magnetic ground state in the (111)-oriented CRO/CMO superlattices. SQUID magnetometry and PNR confirm enhanced emergent magnetization, while EELS and XAS demonstrate a larger shift in Mn valence relative to (001)-oriented samples. Evidence of different Mn valences in the center and interfacial CMO, coupled with XAS line shapes supporting Mn^{2+}, Mn^{3+}, and Mn^{4+} provide hints of a new charge-disproportionated ground state induced by enhanced electron transfer. A more detailed thickness-dependent STEM/EELS study of the thickness-dependent structure and valence would shed light on this question. The shift in Mn valence is unlikely to originate from Mn−Ru intermixing, as CRO/CMO alloys do not exhibit valences below $Mn^{3.6+}$.[26] Further, there is no evidence of greater interfacial alloying with increasing thickness, since the CRO/CMO interfacial roughness measured through AFM, XRR, and PNR is similar across all SLs. Further, T_C in an alloy would be expected to vary with the degree of intermixing but is instead independent of layer thickness, while the net moment doubles. Rather, we suggest that the increased charge transfer is due to the strain state at the (111) interface, where increased interfacial connection between CRO and CMO constrains octahedral tilting as compared to the (001) interface. This increased charge transfer at the (111) interfaces enhances emergent ferromagnetism. PNR, magnetometry, and DFT calculations all suggest a contribution to the emergent ferromagnetism from a weak magnetization of the Ru, with some ambiguity regarding the spatial extent of this induced moment. Theory and PNR favor a rapid decay away of induced CRO moment from the interface with CMO, while magnetometry reveals an increase in magnetization with CRO thickness, which persists up to 15 CRO unit cells.

In this work, we demonstrated massive enhancement of the emergent interfacial magnetization and ordering temperature in CRO/CMO superlattices through interfacial symmetry modification. By growing the superlattices on (111)-oriented substrates rather than (001), the net magnetization is enhanced by nearly a factor or three. Through comprehensive multimodal characterization and calculations, we can attribute this enhancement not to increased intermixing but rather to modifications in the interface symmetry, which alters octahedral connectivity and hence exchange interactions. These results illustrate the power of interface symmetry in controlling the magnetic ground state in quantum materials and correlated electron systems, opening a new pathway for stabilizing novel phases of matter.

■ ASSOCIATED CONTENT

Supporting Information

The Supporting Information is available free of charge at https://pubs.acs.org/doi/10.1021/acs.nanolett.3c04623.

Methods of sample synthesis, structural, chemical, magnetic, and transport characterizations; additional results on X-ray reflectivity, scanning transmission electron microscopy imaging, polarized neutron reflectivity, electrical trasnport, and theoretical calculations (PDF)

■ AUTHOR INFORMATION

Corresponding Authors

Margaret Kane − *Department of Materials Science and Engineering and Geballe Laboratory for Advanced Materials, Stanford University, Stanford, California 94305, United States*; orcid.org/0000-0003-3259-2031; Email: mmkane@stanford.edu

Churna Bhandari − *Ames National Laboratory, Iowa State University, Ames, Iowa 50011, United States*; orcid.org/0000-0002-4380-0732; Email: cbb@ameslab.gov

Yuri Suzuki − *Department of Applied Physics and Geballe Laboratory for Advanced Materials, Stanford University, Stanford, California 94305, United States*; orcid.org/0000-0002-6883-4293; Email: ysuzuki1@stanford.edu

Authors

Megan E. Holtz − *Metallurgical and Materials Engineering, Colorado School of Mines, Golden, Colorado 80401, United States*

https://doi.org/10.1021/acs.nanolett.3c04623
Nano Lett. 2024, 24, 2567−2573

Purnima P. Balakrishnan − *NIST Center for Neutron Research, National Institute of Standards and Technology, Gaithersburg, Maryland 20899, United States;* orcid.org/0000-0002-1426-669X

Alexander J. Grutter − *NIST Center for Neutron Research, National Institute of Standards and Technology, Gaithersburg, Maryland 20899, United States;* orcid.org/0000-0002-6876-7625

Michael Fitzsimmons − *Neutron Scattering Division, Oak Ridge National Laboratory, Oak Ridge, Tennessee 37830, United States*

Chao-Yao Yang − *Department of Material Science and Engineering, National Yang Ming Chiao Tung University, Hsinchu City 30100, Taiwan*

Sashi Satpathy − *Department of Physics & Astronomy, University of Missouri, Columbia, Missouri 65211, United States*

Durga Paudyal − *Ames National Laboratory, Iowa State University, Ames, Iowa 50011, United States; Department of Electrical and Computer Engineering, Iowa State University, Ames, Iowa 50011, United States*

Complete contact information is available at: https://pubs.acs.org/10.1021/acs.nanolett.3c04623

Notes

The authors declare no competing financial interest.

■ ACKNOWLEDGMENTS

The research was supported by the U.S. Department of Energy, Director, Office of Science, Office of Basic Energy Sciences, Division of Materials Sciences and Engineering under Contract No. DESC0008505. A portion of this research used resources at the MAGREF beamline at the Spallation Neutron Source, a DOE Office of Science User Facility operated by the Oak Ridge National Laboratory. Part of this work was performed at the Stanford Nano Shared Facilities (SNSF), supported by the National Science Foundation under Award No. EECS-1542152. This material is based upon work supported by the National Science Foundation Graduate Research Fellowship Grant No. DGE-1656518. Certain commercial equipment, instruments, software, or materials are identified in this work in order to specify the experimental procedure adequately. Such identifications are not intended to imply recommendation or endorsement by NIST, nor it is intended to imply that the materials or equipment identified are necessarily the best available for the purpose. Theoretical and computational research was conducted at Ames National Laboratory for the U. S. DOE with Iowa State University under Contract No. DE-AC02−07CH11358. Work at National Yang Ming Chiao Tung University was supported by NSTC 112-2112-M-A49-026.

■ REFERENCES

(1) Gong, C.; Li, L.; Li, Z.; Ji, H.; Stern, A.; Xia, Y.; Cao, T.; Bao, W.; Wang, C.; Wang, Y.; Qiu, Z. Q.; Cava, R. J.; Louie, S. G.; Xia, J.; Zhang, X. Discovery of intrinsic ferromagnetism in two-dimensional van der Waals crystals. *Nature* **2017**, *546*, 265−269.

(2) Huang, B.; Clark, G.; Navarro-Moratalla, E.; Klein, D. R.; Cheng, R.; Seyler, K. L.; Zhong, D.; Schmidgall, E.; McGuire, M. A.; Cobden, D. H.; Yao, W.; Xiao, D.; Jarillo-Herrero, P.; Xu, X. Layer-dependent ferromagnetism in a van der Waals crystal down to the monolayer limit. *Nature* **2017**, *546*, 270−273.

(3) Huang, B.; Clark, G.; Klein, D. R.; MacNeill, D.; Navarro-Moratalla, E.; Seyler, K. L.; Wilson, N.; McGuire, M. A.; Cobden, D. H.; Xiao, D.; Yao, W.; Jarillo-Herrero, P.; Xu, X. Electrical control of 2D magnetism in bilayer CrI3. *Nat. Nanotechnol.* **2018**, *13*, 544−548.

(4) Jiang, S.; Li, L.; Wang, Z.; Mak, K. F.; Shan, J. Controlling magnetism in 2D CrI3 by electrostatic doping. *Nat. Nanotechnol.* **2018**, *13*, 549−553.

(5) Boschker, H.; et al. Ferromagnetism and Conductivity in Atomically Thin $SrRuO_3$. *Phys. Rev. X* **2019**, *9*, No. 011027.

(6) Cui, Z.; et al. Correlation-driven eightfold magnetic anisotropy in a two-dimensional oxide monolayer. *Sci. Adv.* **2020**, *6*, eaay0114.

(7) Takahashi, K. S.; Kawasaki, M.; Tokura, Y. Interface ferromagnetism in oxide superlattices of $CaMnO_3$ /$CaRuO_3$. *Appl. Phys. Lett.* **2001**, *79*, 1324−1326.

(8) Freeland, J. W.; Chakhalian, J.; Boris, A. V.; Tonnerre, J.-M.; Kavich, J. J.; Yordanov, P.; Grenier, S.; Zschack, P.; Karapetrova, E.; Popovich, P.; et al. Charge transport and magnetization profile at the interface between the correlated metal $CaRuO_3$and the antiferromagnetic insulator $CaMnO_3$. *Phys. Rev. B* **2010**, *81*, No. 094414.

(9) He, C.; Grutter, A. J.; Gu, M.; Browning, N. D.; Takamura, Y.; Kirby, B. J.; Borchers, J. A.; Kim, J. W.; Fitzsimmons, M. R.; Zhai, X.; et al. Interfacial Ferromagnetism and Exchange Bias in $CaRuO_3$ /$CaMnO_3$ Superlattices. *Phys. Rev. Lett.* **2012**, *109*, 197202.

(10) Grutter, A. J.; Vailionis, A.; Borchers, J. A.; Kirby, B. J.; Flint, C. L.; He, C.; Arenholz, E.; Suzuki, Y. Interfacial Symmetry Control of Emergent Ferromagnetism at the Nanoscale. *Nano Lett.* **2016**, *16*, 5647−5651.

(11) Grutter, A.; Kirby, B.; Gray, M.; Flint, C.; Alaan, U.; Suzuki, Y.; Borchers, J. Electric Field Control of Interfacial Ferromagnetism in $CaMnO_3$ /$CaRuO_3$ Heterostructures. *Phys. Rev. Lett.* **2015**, *115*, No. 047601.

(12) Nanda, B. R. K.; Satpathy, S.; Springborg, M. S. Electron Leakage and Double-Exchange Ferromagnetism at the Interface between a Metal and an Antiferromagnetic Insulator: $CaRuO_3$ /$CaMnO_3$. *Phys. Rev. Lett.* **2007**, *98*, 216804.

(13) He, C.; Zhai, X.; Mehta, V. V.; Wong, F. J.; Suzuki, Y. Interfacial magnetism in $CaRuO_3$ /$CaMnO_3$ superlattices grown on (001) $SrTiO_3$. *J. Appl. Phys.* **2011**, *109*, No. 07D729.

(14) Flint, C. L.; Vailionis, A.; Zhou, H.; Jang, H.; Lee, J.-S.; Suzuki, Y. Tuning interfacial ferromagnetism in $LaNiO_3$/$CaMnO_3$superlattices by stabilizing nonequilibrium crystal symmetry. *Phys. Rev. B* **2017**, *96*, No. 144438.

(15) Hallsteinsen, I.; Moreau, M.; Grutter, A.; Nord, M.; Vullum, P.-E.; Gilbert, D. A.; Bolstad, T.; Grepstad, J.; Holmestad, R.; Selbach, S.; et al. Concurrent magnetic and structural reconstructions at the interface of (111)-oriented $La_{0.7}$ $Sr_{0.3}$ MnO_3 /$LaFeO_3$. *Phys. Rev. B* **2016**, *94*, 201115.

(16) Hallsteinsen, I.; Grutter, A.; Moreau, M.; Slöetjes, S. D.; Kjærnes, K.; Arenholz, E.; Tybell, T. Role of antiferromagnetic spin axis on magnetic reconstructions at the (111)-oriented $La_{0.7}$ $Sr_{0.3}$ MnO_3 /$LaFeO_3$ interface. *Physical Review Materials* **2018**, *2*, No. 084403.

(17) Caspi, E. N.; Avdeev, M.; Short, S.; Jorgensen, J. D.; Lobanov, M. V.; Zeng, Z.; Greenblatt, M.; Thiyagarajan, P.; Botez, C. E.; Stephens, P. W. Structural and magnetic phase diagram of the two-electron-doped $(Ca_{1-x}Ce_x)MnO_3$system: Effects of competition among charge, orbital, and spin ordering. *Phys. Rev. B* **2004**, *69*, 104402.

(18) Wollan, E. O.; Koehler, W. C. Neutron Diffraction Study of the Magnetic Properties of the Series of Perovskite-Type Compounds [(1 − *x*)La, xCa]MnO_3. *Phys. Rev.* **1955**, *100*, 545−563.

(19) He, T.; Cava, R. J. The effect of Ru-site dopants on the magnetic properties of $CaRuO_3$. *J. Phys.: Condens. Matter* **2001**, *13*, 8347−8361.

(20) Maignan, A.; Martin, C.; Hervieu, M.; Raveau, B. Ferromagnetism and metallicity in the $CaMn_{1-x}$ Ru_x O_3 perovskites: a highly inhomogeneous system. *Solid state communications* **2001**, *117*, 377−382.

(21) Mizusaki, S.; Taniguchi, T.; Okada, N.; Nagata, Y.; Hiraoka, N.; Itou, M.; Sakurai, Y.; Noro, Y.; Ozawa, T. C.; Samata, H. Magnetic

ground states of $CaRu_{1-x}$ Mn_x O_3 ($0.2 \leq x \leq 0.9$): a magnetic Compton scattering study. *J. Phys.: Condens. Matter* **2009**, *21*, 276003.
(22) Kawanaka, H.; Yokoyama, M.; Noguchi, A.; Bando, H.; Nishihara, Y. Itinerant electron magnetism in $CaRu_{1-x}$ Mn_x O_3 ($0 \leq x \leq 0.5$). *J. Phys.: Condens. Matter* **2009**, *21*, 296002.
(23) Flint, C. L.; Yi, D.; Karapetrova, E.; N'Diaye, A. T.; Shafer, P.; Arenholz, E.; Suzuki, Y. Enhanced interfacial ferromagnetism and exchange bias in (111)-oriented $LaNiO_3/CaMnO_3$ superlattices. *Physical Review Materials* **2019**, *3*, No. 064401.
(24) Chmaissem, O.; Dabrowski, B.; Kolesnik, S.; Mais, J.; Brown, D. E.; Kruk, R.; Prior, P.; Pyles, B.; Jorgensen, J. D. Relationship between structural parameters and the Néel temperature in $Sr_{1-x}Ca_xMnO_3(0x1)$and $Sr_{1-y}Ba_yMnO_3(y0.2)$. *Phys. Rev. B* **2001**, *64*, 134412.
(25) Bhandari, C.; Satpathy, S. Dielectric screening and electric field control of ferromagnetism at the $CaMnO_3$ /$CaRuO_3$ interface. *Phys. Rev. B* **2021**, *104*, No. 085134.
(26) Zhou, Q.; Kennedy, B. J.; Zhang, Z.; Jang, L.-Y.; Aitken, J. B. X-ray Absorption near Edge Structure and Crystallographic Studies of the Mixed Valence Oxides CaRu1- x Mn x O3. *Chem. Mater.* **2009**, *21*, 4203−4209.

https://doi.org/10.1021/acs.nanolett.3c04623
Nano Lett. 2024, 24, 2567−2573